Materials Characterization 96 (2014) 256–262

Contents lists available at ScienceDirect

Materials Characterization

journal homepage: www.elsevier.com/locate/matchar

Structures in textured Cu–Al–Ni shape memory thin films grown by sputtering

C. Espinoza Torres [a,b], A.M. Condó [a,b,*], N. Haberkorn [a,b], E. Zelaya [a,b], D. Schryvers [c], J. Guimpel [a,b], F.C. Lovey [a]

[a] *Centro Atómico Bariloche, Comisión Nacional de Energía Atómica, 8400 S.C. de Bariloche, Argentina*
[b] *Consejo Nacional de Investigaciones Científicas y Técnicas, Argentina*
[c] *EMAT, University of Antwerp, Belgium*

ARTICLE INFO

Article history:
Received 6 June 2014
Received in revised form 6 August 2014
Accepted 7 August 2014
Available online 10 August 2014

Keywords:
Thin films
Microstructure
Shape memory

ABSTRACT

The structure and texture formation in Cu–Al–Ni thin films of different thicknesses (1 μm to 5 μm) grown by DC magnetron sputtering without any intentional heating of the substrate are reported. The as-grown films present grains with an average size of 20 nm. The films with thickness of 1 μm have a single metastable phase with a hexagonal structure and are textured with planes (0002) parallel to the plane of the films. It was observed that thicker films present phase coexistence between metastable hexagonal and body centered cubic structures with a gradual increment of the body centered cubic phase fraction. The films with thickness of 5 μm are textured with planes (0002) and $\left\{10\bar{1}0\right\}$ in the hexagonal structure, whereas in the body centered cubic structure the films are textured with {110} planes parallel to the plane of the films. This fact can be associated with self-heating of the substrate during the growth of the films and with the relative stability of the metastable phases. Free standing films annealed in a second step (1123 K for 1 h) present austenitic phase with $L2_1$ structure and sub-micrometric grains textured with $\{220\}_{L21}$ planes parallel to the plane of the films. The martensitic transformation temperature was determined from the analysis of resistance against temperature measurements.

1. Introduction

Shape-memory alloys (SMAs) undergo reversible changes in their crystallographic structure, depending on the temperature and stress state. These changes are based on a thermoelastic reversible martensitic transformation between an austenitic phase (high temperature) and a martensitic phase (low temperature). The shape memory effect refers to the possibility of these materials to recover their original shape by increasing their temperature into the austenite, after being deformed in the martensite. This effect has been successfully adopted in a broad set of advanced and innovative applications, which include the development of micro-electromechanical systems (MEMS) [1–3]. For this purpose, SMA thin films have been grown using different techniques such as evaporation, sputtering and electrodeposition [4–7]. Among all SMAs, films of NiTi-based alloys have been extensively studied [2]. The performance of low dimensional systems is strongly affected by the nature of the martensitic transformation and by their microstructure. Recently, high mechanical performance has been reported in single crystalline Cu–Al–Ni nanopillars [8] obtained by focused ion beam (FIB). Also in bulk systems, the martensitic transformation and mechanical properties in Cu–Al–Ni are strongly dependent on the microstructure. Cu–Al–Ni alloys exhibit an excellent shape memory effect in single crystalline states, but they present brittle fracture along the grain boundaries in polycrystalline states [9]. One way to improve their mechanical properties is reducing the grain size, which in thin films can be achieved by modifying the growth parameters [10].

Depending on processing conditions, SMA thin films can be deposited at room temperature or high temperatures. Films obtained at room temperature need a post-sputtering annealing process (the temperature depends on the equilibrium temperature of the austenitic β phase). The resulting properties, such as martensitic transformation temperatures and its features (hysteresis and extension), depend on the actual procedure. For example, it was found that the grain size in Cu–Al–Ni thin films obtained by sputtering decreases with lower substrate temperatures and lower chamber Ar gas pressure [10]. For a substrate temperature of 473 K and 4 Pa partial pressure of Ar, the films present grains with diameters of around 500 nm and are ordered in the DO_3 structure. These films show shape memory effect but poor bending ductility. Nanometric grains in Cu–Al–Ni thin films can also be obtained by sputtering without any intentional heating of the substrate [4]. The as-grown films show phase coexistence of textured hexagonal (Hex) and body centered cubic (BCC) structures. The shape memory effect appears after a process of heating the films up to 1073 K followed by water quenching. The martensitic transformation temperature (M_s) of Cu–Al–Ni alloys ranges between 70 and 470 K depending on the chemical concentration. At Al contents above

---

* Corresponding author at: Centro Atómico Bariloche, Comisión Nacional de Energía Atómica, 8400 S.C. de Bariloche, Argentina.
E-mail address: adriana@cab.cnea.gov.ar (A.M. Condó).

http://dx.doi.org/10.1016/j.matchar.2014.08.005
1044-5803/

13 wt.%, the parent β phase transforms to an ordered phase, having a $L2_1$-type superlattice, prior to the transformation [11]. The thermally induced martensitic phase obtained undergoes an evolution from monoclinic 18R to orthorhombic 2H with the increase of Al concentration. Several authors have reported DO_3 as the order of the austenitic structure in Cu–Al–Ni alloys. However, it is considered that $L2_1$ describes the order in these alloys more accurately. The difference between DO_3 and $L2_1$ is not relevant to this paper and only the $L2_1$ structure will be considered [12,13].

In this work the structures and crystal texture in Cu–Al–Ni thin films with different thicknesses were studied using transmission electron microscopy (TEM) of plan-view and side-view specimens and X-ray diffraction (XRD). The films were grown by DC magnetron sputtering without any intentional heating of the substrate. The results show that the films obtained at room temperature present a phase coexistence of textured Hex and BCC structures. After annealing, textured $\{220\}_{L21}$ Cu–Al–Ni thin films with sub-micrometric grains were obtained. It was found that the final texture present in the annealed films is due to recrystallization in the as-grown Hex and BCC structures. The presence of martensitic transformation in the annealed films was observed by electrical resistance measurements.

2. Material and Methods

The target for sputtering was prepared from a high purity alloy of Cu–27.35 at.% Al–5.45 at.% Ni melted in an induction furnace under Ar atmosphere. The martensitic transformation temperature of the target was $M_S = 250$ K and the hysteresis width was around 10 K. Films with thickness of ≈ 5 μm were grown on Si (100) by DC magnetron sputtering from the target with an applied power of 50 W. The sputtering gas was Ar at a pressure of 10 mTorr. During the sputtering process the substrate was right above the target at a distance of ≈ 7 cm. The deposition rate was calibrated by surface profile measurements, giving a rate of 50 nm min^{-1}. The films were grown without any intentional heating of the substrate. Self-heating to approximately 420 K was induced by the sputtering process, as measured by a thermocouple inside the substrate holder. After deposition, the films were easily peeled off from the substrate. The samples were wrapped in tantalum foils and encapsulated in a quartz tube with Ar atmosphere. Finally, they were annealed during 1 h at 1123 K and fast quenched in ice water. Films with final thicknesses of 1.0 (0.1) μm, 1.5 (0.1) μm and 5.0 (0.3) μm were obtained.

The structures and microstructures of the as-grown films were analyzed by XRD and TEM. The room temperature XRD data were obtained using a Philips PW 1820 diffractometer. XRD patterns (as a function of temperature) were obtained in a commercial sample holder mounted in a Panalytical Empyrean equipment. TEM results were obtained using a Philips CM 200UT microscope operated at 200 kV. Plan-view and side-view (cross-section) TEM specimens of the free standing as-grown films were obtained by electropolishing and focused ion beam (FIB) in a FEI Quanta 200 dual-beam system, respectively. In annealed films, plan-view specimens were obtained by ion thinning and cross-sections by FIB in a FEI Helios NanoLab 650 system. The preparation of the TEM lamella by FIB was done with low current and voltage in the last steps in order to avoid the formation of additional phases and also to minimize the ion beam damage to the thin section [14].

The presence of shape memory in the annealed 5.0 μm thick Cu–Al–Ni films was confirmed through mechanical deformation. The characteristic temperatures (austenite start (A_s), austenite finish (A_f), martensite start (M_s) and martensite finish (M_f)) were parameterized by performing resistance versus temperature measurements with the conventional four-probe geometry. The martensitic transformation in the films with thickness of 1 and 1.5 μm was not determined due to the presence of buckling, which hampers the manipulation of the thin films.

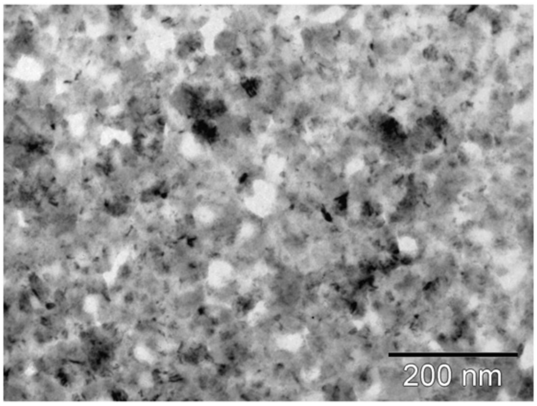

Fig. 1. Bright field image of the as-grown 5 μm thin film in plan-view orientation.

3. Results

3.1. Microstructure of the As-grown Films

Fig. 1 shows a bright field plan-view TEM image of a film with a thickness of 5 μm. The image shows a complex microstructure with an average grain diameter of 20 nm. Complementary nanodiffraction patterns were obtained in a film with an original thickness of 5 μm to identify the main crystalline orientations of the grains in the plan-view specimens (see Fig. 2). The following structures and orientations could be determined: $[0001]_{\text{Hex}}$, $\langle 10\bar{1}0\rangle_{\text{Hex}}$ and $\langle 1\bar{1}0\rangle_{\text{BCC}}$ (Fig. 2a, b and c, respectively), with the first one the most frequent. In Fig. 2c, only fundamental reflections corresponding to the BCC structure are observed, and no superlattices such as B2 or $L2_1$ were found. The results show that the films obtained at room temperature present a phase coexistence of Hex and BCC structures.

Selected area diffraction (SAD) patterns exhibit uniform rings due to the polycrystalline nature. Fig. 3 shows images of the diffraction rings processed by FIT2D [15], to transform rings in straight lines, and ACC software [16], to enhance faint reflections. One diffraction pattern corresponds to a film with thickness of 1 μm (left) and the other one to a film with thickness of 5 μm (right). Columns a, b and c in Fig. 3 include all the expected reflection rings corresponding to the Hex and BCC structures with $[0001]_{\text{Hex}}$, $\langle 10\bar{1}0\rangle_{\text{Hex}}$ and $\langle 1\bar{1}0\rangle_{\text{BCC}}$ texture, respectively. As seen in Fig. 3, with $[0001]_{\text{Hex}}$ texture the rings in the film with a thickness of 1 μm can be completely indexed. After tilting the TEM plan-view specimen, SAD patterns show incomplete rings, which indicate the presence of texture (not shown).

Fig. 4 shows a TEM cross-section analysis of the 5 μm thick Cu–Al–Ni film. Fig. 4a shows a dark field image where columnar grains along the growth direction (n) are observed. The dark field image was obtained from the main reflection in the diffraction pattern, labeled as 0002_{Hex} in Fig. 4b, parallel to the normal direction. The electron diffraction pattern from the cross-section specimen was reproduced three times to index different textures (Fig. 4b, c and d). It was processed with the ACC software routines [16], with a setting that allowed contrast enhancement for weak reflections. Intensity arcs of about 15° coming from incomplete rings were observed, compatible with the texture of the film. The main reflection used for dark field imaging (indicated as 0002_{Hex}, $10\bar{1}0_{\text{Hex}}$ and $1\bar{1}0_{\text{BCC}}$ in Fig. 4b, c and d, respectively) was composed of three reflections according to the orientations observed by nanodiffraction. Diffraction patterns including these reflections were identified and simulated with the JEMS package software [17]. The zone axes $[\bar{1}2\bar{1}0]_{\text{Hex}}$ and $[10\bar{1}0]_{\text{Hex}}$ have the common reflection 0002_{Hex}, and contribute to several diffraction arcs as indicated in Fig. 4b by squares and rhombus, respectively. Similarly, the zone

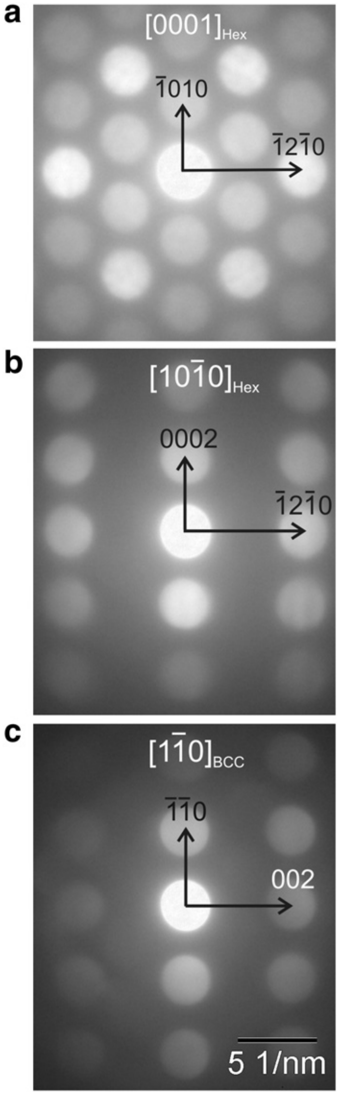

Fig. 2. Nanodiffraction patterns observed in plan-view specimens of the 5 μm films. a) $[0001]_{Hex}$. b) $\left[10\bar{1}0\right]_{Hex}$. c) $\left[1\bar{1}0\right]_{BCC}$.

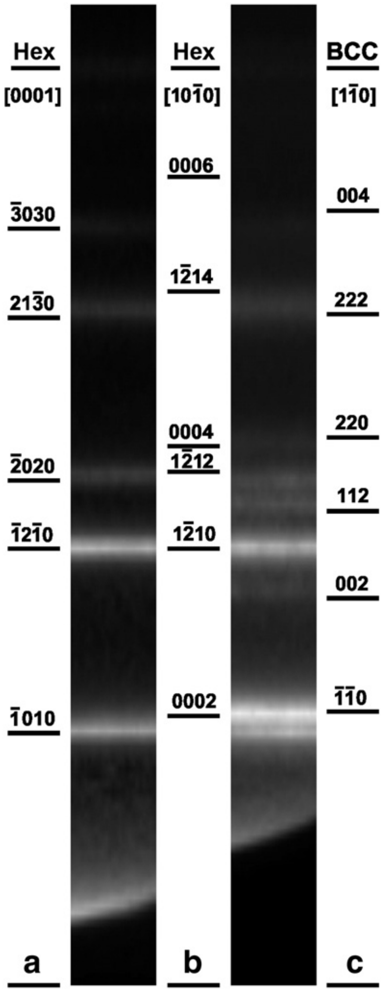

Fig. 3. Electron diffraction ring patterns of the as-grown 1 μm film (left) and 5 μm film (right), transformed to straight lines. Columns a, b and c: key diagrams of the reflections corresponding to the $[0001]_{Hex}$, $\left[10\bar{1}0\right]_{Hex}$ and $\left[1\bar{1}0\right]_{BCC}$ orientations.

axes $[\bar{1}2\bar{1}0]_{Hex}$, $[0001]_{Hex}$ and $[\bar{2}4\bar{2}3]_{Hex}$ have the common reflection $10\bar{1}0_{Hex}$, and contribute to additional diffraction arcs as indicated in Fig. 4c by squares, rhombus and circles, respectively. Finally, the zone axes $[001]_{BCC}$, $[110]_{BCC}$, $[111]_{BCC}$, $[113]_{BCC}$ and $[331]_{BCC}$ have the common reflection $1\bar{1}0_{BCC}$ and explain most of the remaining diffraction arcs in Fig. 4d. A few reflections remain unidentified, as for instance the arc indicated with an arrow in Fig. 4b. Nevertheless, it can be concluded that nearly all reflections in the electron diffraction pattern of the cross-section specimen can be explained taking into account the same texture obtained by nanodiffraction in Fig. 2. It is important to mention that the rocking curve around the main peak has a full width at half maximum (FWHM) ≈8° (not shown) which is consistent with the texture obtained from TEM data.

Fig. 5 shows the intensity as a function of the inverse interplanar distance of the XRD pattern and the electron diffraction pattern profile along the normal direction of the 5 μm thin film. The data provide information along the vertical direction across the origin in Fig. 4b. In the inset, a detail of the main peak at 4.72 nm^{-1} is shown. A good agreement between both diffraction data is observed, which indicates the absence of FIB induced major artifacts in the specimen. This allowed a precise calibration of the electron diffraction pattern in relation with the XRD results. The main peak at 4.72 nm^{-1} is indexed according to three reflections 0002_{Hex}, $10\bar{1}0_{Hex}$ and $1\bar{1}0_{BCC}$.

The lattice parameters (as obtained from the XRD and TEM data) for the BCC and Hex structures are: $a_{BCC} = (0.295 \pm 0.005)$ nm, $a_{Hex} = (0.26 \pm 0.01)$ nm and $c_{Hex} = (0.423 \pm 0.002)$ nm. The reported lattice parameter for the Cu–Al–Ni austenite (β phase) is $a_{\beta} = 0.5836$ nm [18]. Ignoring the superlattice structure, the lattice parameter would be $a_{\beta} / 2 = 0.292$ nm. Within the experimental error this value is the same as the one obtained in this work for the BCC structure. The reported lattice parameters of the martensite with 2H structure are $a_{2H} = 0.439$ nm, $b_{2H} = 0.534$ nm and $c_{2H} = 0.422$ nm [19]. Ignoring the superlattice structure and the orthorhombic distortion of the 2H basal plane, an Hex structure is obtained with lattice parameters $a = 0.260$ nm and $c = 0.422$ nm, which are remarkably similar to the values of the Hex metastable phase observed in this work.

Fig. 6 shows a comparison of the XRD data obtained in Cu–Al–Ni thin films of different thicknesses (1 μm, 1.5 μm and 5 μm). It is important to mention that the reflection corresponding to the BCC phase is only present in thicker films. This fact implies that the BCC structure appears as a consequence of long time growth, and it can be associated with self-heating (≈420 K) during the sputtering process. XRD patterns were also performed on the top and bottom surfaces of the 5 μm film (not shown). It was noticed that there are no major differences between both surfaces (Hex and BCC structures), which indicates that self-

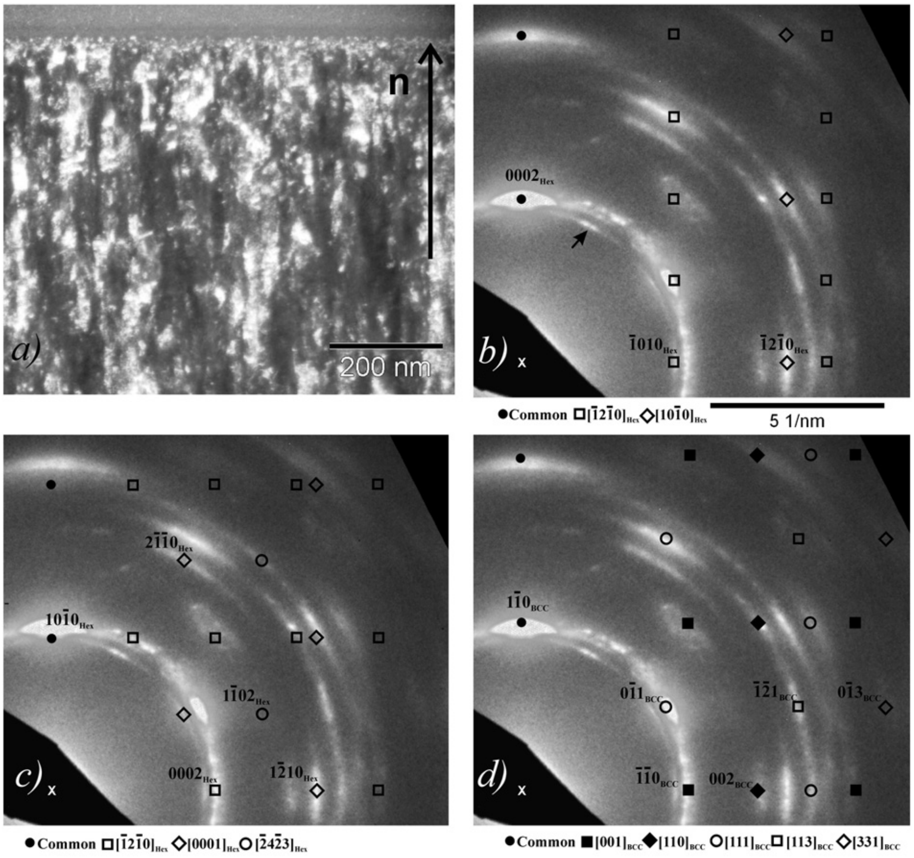

Fig. 4. Microstructure and electron diffraction pattern of the 5 μm thin film in the cross-section specimen. a) Dark field image with reflection 0002_{Hex}. The normal (n) of the surface is parallel to the growing direction. b) Corresponding diffraction pattern with identification of reflections from zone axes that contribute to: 0002_{Hex}, c) $10\bar{1}0_{Hex}$, d) $1\bar{1}0_{BCC}$ reflections.

heating (longer deposition times) produces a reconstructive phase transformation Hex → BCC structures.

3.2. Temperature Evolution of the Microstructure

As discussed above, the as-grown Cu–Al–Ni films present coexistence of Hex and BCC metastable phases. At 773 K the equilibrium phases for Cu–Al–Ni are mainly α (Cu) and γ_2 (Cu_9Al_4) [20]. Fig. 7 shows the XRD patterns corresponding to the thermal evolution of the crystalline phases in an as-grown 5 μm thick Cu–Al–Ni film. The XRD patterns were obtained at constant temperature. Between each successive measurement the temperature increase was 50 K/min. Fig. 7a shows a comparison between the XRD pattern obtained in an as-grown film (equivalent to that shown in Fig. 6), and the one obtained after heating the sample to 523 K. The results show an increment of the $1\bar{1}0_{BCC}$ peak corresponding to the BCC phase, which suggests that small changes in the sample temperature produce a reconstructive Hex → BCC phase transformation. Both metastable phases are decomposed at around 673 K in the equilibrium α and γ_2 phases (see Fig. 7b). Sharp peaks can be observed due to recrystallization. It is important to mention that, from the XRD pattern, it is difficult to differentiate 111_α (Cu) from 0002_{Hex} peaks. When the temperature is increased at around 973 K (see Fig. 7c), the α and γ_2 phases transform to the equilibrium β phase with $L2_1$ structure (see the next section). Finally, if the

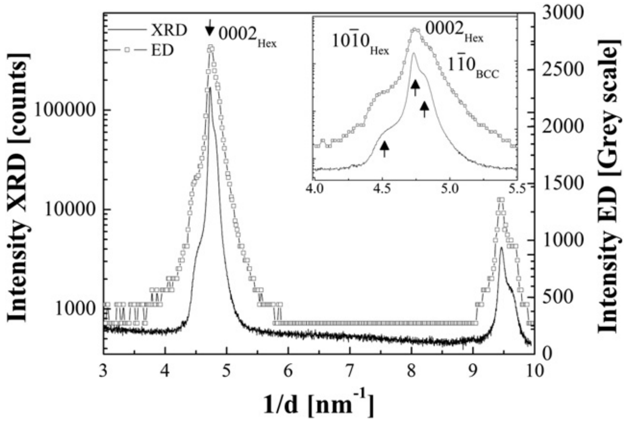

Fig. 5. Comparison of the intensity of the X-ray diffraction (XRD) pattern with the electron diffraction (ED) in the plan-view specimen of the 5 μm as-grown films. See details of the main peak in the inset.

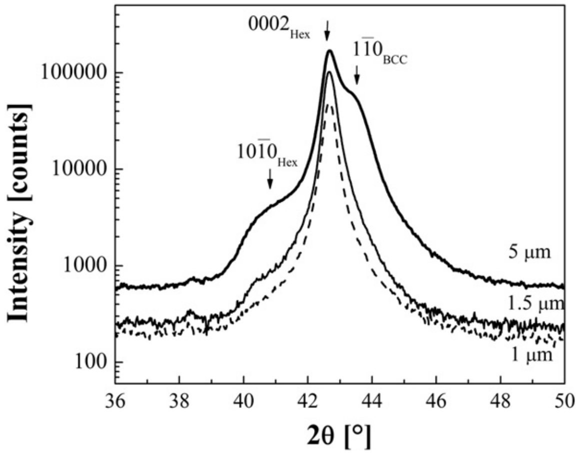

Fig. 6. Comparison of the intensity of X-ray diffraction data for as-grown thin films with a thickness of about 5 μm, 1.5 μm and 1 μm.

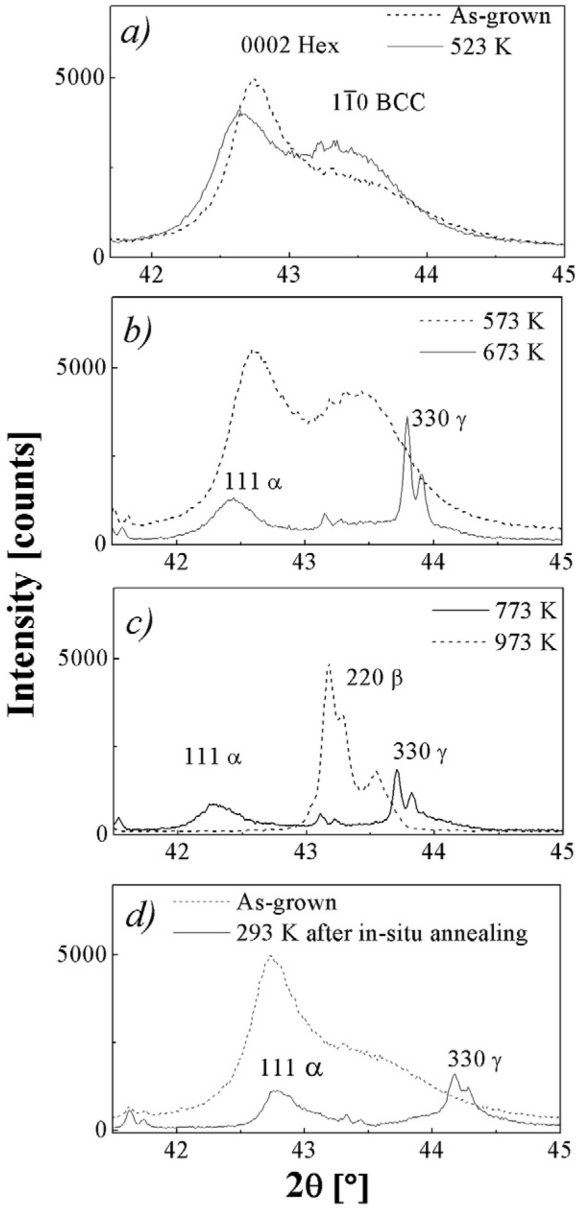

Fig. 7. X-ray diffraction pattern of a 5 μm thick as grown Cu–Al–Ni film as a function of temperature. a) As-grown and 523 K. b) 573 and 673 K. c) 773 K and 973 K. d) As-grown and 293 K after cooled down from 973 K.

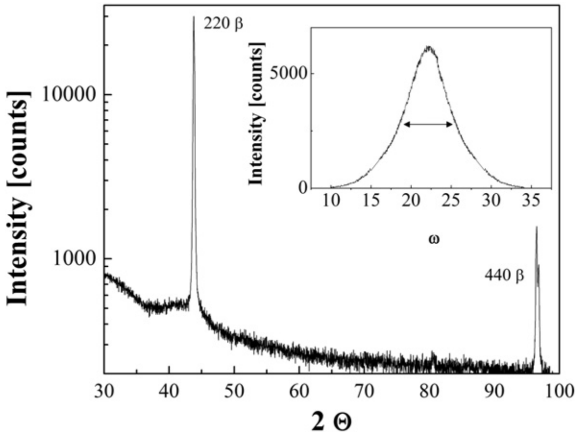

Fig. 8. X-ray diffraction pattern of the Cu–Al–Ni film after annealing. Inset: Rocking curve around the 220 peak.

sample is cooled down by turning off the heater, α and γ_2 phases appear in contrast with the initially present Hex and BCC metastable phases (see Fig. 7d). The fast thermal decomposition of the β phase, indicates that fast quenching is necessary in order to obtain a pure austenitic phase.

3.3. Resulting Microstructure and Martensitic Transformation After Annealing

According to the results presented in Section 3.2, the thermal annealing and fast quenching are of great importance in the resulting crystalline phases present in the sample. In order to avoid thermal decomposition during the annealing (α and γ_2 precipitation), the encapsulated film was immediately introduced in a furnace at 1123 K for 1 h. Then, it was fast quenched in ice water. Fig. 8 shows the XRD of the 5 μm thick film after the procedure formerly described. Only peaks 220 and 440 corresponding to the $L2_1$ structure of the β phase are observed. The rocking curve FWHM of the 220 peak (see Fig. 8 inset) was ≈7°, which indicates that the texture initially present in the as-grown film contributes to the final microstructure. It is important to mention that the recrystallization process produced during the thermal annealing is different from the one present in Cu–Zn–Al, where the texture initially present in the as-grown film disappears [7].

Fig. 9 shows the microstructure of the annealed film in plan-view and side-view. From both views in bright field TEM images (Fig. 9a and c) the same microstructure is observed indicating equiaxed grains inside the film. Small grains (<500 nm), with a grain size average of around 200 nm were obtained (see Fig. 9b). The electron diffraction pattern of the plan-view image corresponds to the $L2_1$ structure (see Fig. 9a inset). Fig. 9c and d corresponds to the same area observed in bright and dark field images. The electron diffraction pattern (see Fig. 9d inset) shows that the film is textured with the normal of the surface (n) along the $[110]_{L21}$ direction. This is in agreement with the XRD data (Fig. 8).

Fig. 10 shows a comparison between different martensitic transformations obtained from resistance vs. temperature (T) curves. A piece obtained from the target presents an $M_s = 250$ K and a hysteresis ≈ 10 K. The hysteresis of the transformation is close to the value expected for the $L2_1 \rightarrow 18R$ martensitic transformation. The M_s in the film depends on the distance to the center of the sample. The M_s in the center is 60 K lower than on the edges of the sample (≈0.7 mm). Considering similar microstructures, this is consistent with the presence of small chemical gradients in the precursor sputtered film (<1 at.%). The extension of the martensitic transformation (M_s–M_f) > 60 K at the edges could be associated with the presence of these gradients that produce a span of M_s. On the other hand, the hysteresis of the transformation in the films ≈ 35 K is larger than the value obtained from bulk (target), and could be associated with the presence of very small grains that act as obstacles for variant growth [21]. A similar behavior was previously observed in Cu–Zn–Al films with micrometric grains [7], and could be associated with inter-granular stresses inhibiting the propagation of martensitic variants. Even though the overcooling needed to produce the driving force in Cu–Al–Ni films with sub-micrometric grains (200 nm) increases the hysteresis in the transformation, it is lower than in Cu–Zn–Al thin films (≈50 K), with both systems showing an $L2_1 \rightarrow 18R$ transformation.

Finally, it is important to mention that a deformation of approximately 1% was obtained by cooling down the free standing films through the martensitic transformation under a stress of 100 MPa. This deformation is much smaller than the 10% obtained in epitaxial Ni–Mn–Ga films [22] by tensile experiments along the [001] direction.

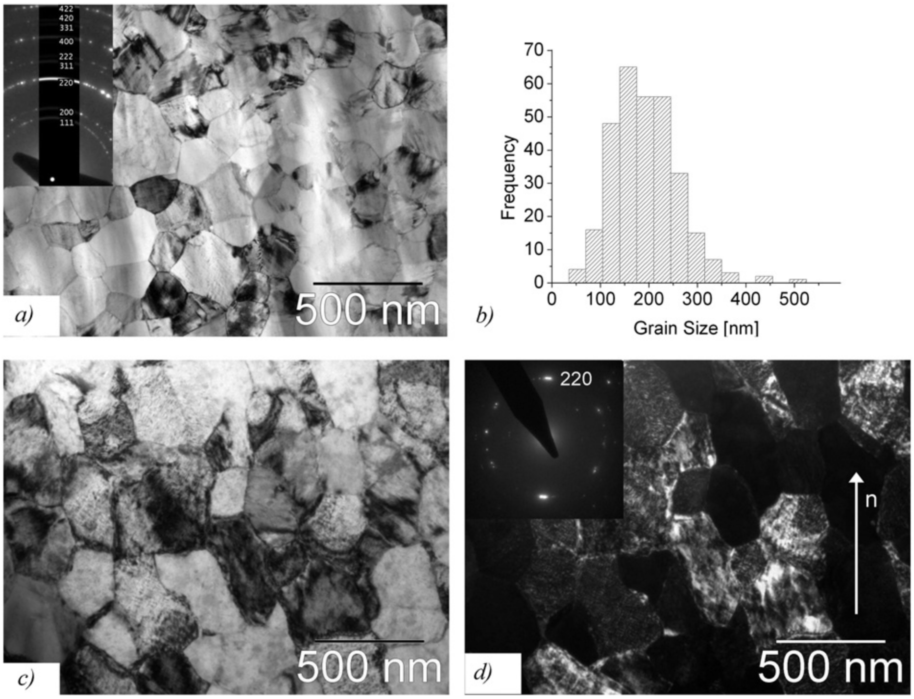

Fig. 9. Microstructure of an annealed Cu–Al–Ni film. a) Bright field TEM image of a plan-view specimen. Inset: Corresponding $L2_1$ diffraction rings. b) Grain size distribution. c) and d) Side view of the film in bright field and 220 dark field image, respectively. The inset in d) shows the corresponding diffraction pattern indicating 220 texture parallel to the normal of the surface (n).

This considerable difference could be attributed to the nature of the martensitic transformation in polycrystals with sub-micrometric grains and single crystals.

4. Discussion

The results show that Cu–Al–Ni films obtained by DC sputtering without any intentional heating of the substrate present textured metastable phases. An Hex structure with (0002) planes parallel to the plane of the films is observed for a film thickness of 1 μm. The presence of this preferential orientation can be understood by taking into account that the lattice planes parallel to the surface are the closest packed planes related to the Hex phase. Thicker films present phase coexistence between metastable Hex and BCC structures. A gradual increment of the BCC phase fraction is observed for longer deposition times, which can be associated with a reconstructive phase transformation [23]. A similar behavior has been observed when as-grown thin films are heated to 573 K. The analysis of the texture initially present is necessary in order to understand the texture present in the annealed films.

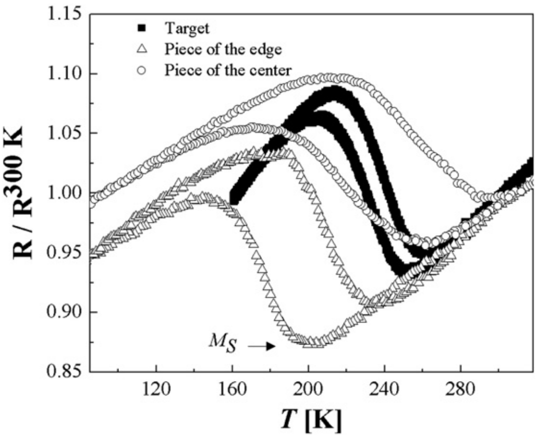

Fig. 10. Normalized resistance vs temperature curves for the target and two pieces (1 cm × 0.1 cm) of a 5 μm thick Cu–Al–Ni film (1 cm × 2 cm).

The as-grown films with thickness of 5 μm are textured with (0002) and $\{10\bar{1}0\}$ planes in the Hex structure and $\{110\}_{BCC}$ in the BCC structure parallel to the plane of the films. This texture indicates that the normal of the films is parallel to the $[0001]_{Hex}$, $\langle 10\bar{1}0\rangle_{Hex}$ and $\langle 110\rangle_{BCC}$ directions (Fig. 2). This correspondence between textures in the BCC and Hex structures could be understood when comparing the crystallographic relationships between the $L2_1$ austenite and 2H martensite (Table 1 (columns 2 and 3)) in Cu-based shape memory alloys [24]. The BCC and Hex structures can be visualized as disordered $L2_1$ and 2H structures, respectively. The correspondence between BCC and $L2_1$ is described in Table 1 (col 1 and 2), whereas the correspondence between Hex and 2H is described in the last two columns of the same table. From Table 1, it is inferred that the $[10\bar{1}0]_{Hex}$ and $[0001]_{Hex}$ directions are in correspondence to the $<110>_{BCC}$ directions. This supports the idea of a reconstructive phase transformation $(0002)_{Hex}\rightarrow(1\bar{1}0)_{BCC}$ and $(1\bar{1}0)_{BCC}\rightarrow(10\bar{1}0)_{Hex}$ among the observed textures and phases.

At 773 K the equilibrium phases for Cu–Al–Ni are mainly α (Cu) and γ_2 (Cu_9Al_4) [20]. At room temperature, the same phases remain stable (Fig. 7). However, these equilibrium phases are not observed in the as grown films. They have different compositions between them and therefore diffusion is needed to allow both phases to appear. In Cu–Al–Ni films grown by sputtering, diffusion effects could be suppressed or minimized by two reasons. On the one hand, the growth is performed at low temperatures and on the other hand, diffusion of Cu and Al is inhibited when Ni is added [9]. As a consequence, the equilibrium phases do not develop and hexagonal and BCC metastable phases appear, with no long range order and with fixed composition similar to the target one.

The disordered phases with FCC, BCC and Hex structures can be found at high temperatures in the Hume–Rothery alloys based on the

Table 1
Crystallographic relationships between the $L2_1$ austenite and 2H martensite in Cu based shape memory alloys compared to the observed texture in metastable phases in Cu–Al–Ni thin films.

Metastable BCC	Austenite $L2_1$ structure (cubic)	Martensite 2H structure (orthorhombic)	Metastable hexagonal
$<110>_{BCC}$	$<110>_{L21}$	$[100]_{2H}$	$\left[10\bar{1}0\right]_{Hex}$
$<110>_{BCC}$	$<110>_{L21}$	$[001]_{2H}$	$[0001]_{Hex}$

noble metals (Cu, Ag and Au). A characteristic sequence of equilibrium phases (which is controlled by the conduction electron concentration *e*/*a* [25]) is present in alloys which contain elements from the right side of the periodic table. The stability of the disordered close packed structures in these alloys was previously analyzed [26]. The free energy differences of the FCC and 9R structures with reference to the Hex structures are given as a function of the electron concentration *e/a*. For *e/a* values above 1.44, the Hex structure is the most stable, whereas for lower *e/a* values the FCC structure is the most stable. These free energy differences were experimentally found to be scarcely dependent on the temperature. In the case of the present alloy, the *e/a* can be calculated considering the nominal composition of the target which results in $e/a = 1.51$. Thus, if no composition change is permitted, the Hex structure would be the most stable, as indeed observed in the as-grown film. Another result which is also in agreement with the stability analysis was observed in Cu–19.5 at.% Al thin films ($e/a = 1.39$) grown by sputtering, where the FCC structure was obtained [7].

The films obtained after annealing at 1123 K for 1 h present shape memory and they could be mechanically deformed [4]. At room temperature, textured $\{220\}_{L21}$ Cu–Al–Ni thin films with sub-micrometric grains were obtained. The texture finally present in the annealed films is due to recrystallization in the as-grown Hex and BCC structures. Therefore, the texture initially present in the as-grown film influences the final microstructure. It is important to mention that no brittle fracture was observed during their manipulation.

The hysteresis corresponding to the martensitic transformation in the annealed Cu–Al–Ni films is smaller than the one found in Cu–Al–Zn films with the same $L2_1 \rightarrow 18R$ martensitic transformation. This fact could be associated with the driving force needed for the martensitic transformation. The driving force ΔG generated by undercooling around the $T_0 = (M_S + A_F)/2$ can be related to the entropy change ΔS between the β phase and the martensite by $\partial \Delta G / \partial T = -\Delta S$. In Cu-based alloys with $L2_1 \rightarrow 18R$ martensitic transformation, the change in the entropy depends on the average of the conduction electrons per atom (*e/a*) [27]. In Cu–Zn–Al $\Delta S = 1.46\ \mathrm{J\ mol^{-1}\ K^{-1}}$ ($e/a = 1.48$) while in Cu–Al–Ni $\Delta S = 1.51\ \mathrm{J\ mol^{-1}\ K^{-1}}$ ($e/a = 1.51$). The entropy change related to the martensitic transformation is larger in Cu–Al–Ni alloys and therefore, less overcooling is necessary to obtain the same driving force. However, this ΔG by itself cannot explain hysteresis differences as large as 15–20 K, which indicates that other effects such as texture are affecting the martensitic transformation in the films.

5. Conclusions

Textured Cu–Al–Ni thin films with micrometric grains have been obtained in two steps: sputtering and post-annealing. The initially present metastable BCC and Hex phases contribute to the final texture obtained in the annealed films. The annealed films show a microstructure with sub-micrometric grains. No brittle behavior was observed during their manipulation. The martensitic transformation presents a larger hysteresis than the one observed in the bulk, which could be associated with the small grain size.

Acknowledgments

The authors would like to thank Dr. Ch. Somsen, Dr. A. Kröger and Dr. J. Rao for TEM sample preparation of as-grown films by FIB at the Institute fur Werkstoffe, RUB, Bohum, Germany; Dr. J. L. Pelegrina for fruitful discussion; and A. Geraci, C. Gómez Bastidas, D. Wilberger, M. Isla and E. Aburto for the technical assistance. Financial support from Consejo Nacional de Investigaciones Científicas y Técnicas of Argentina (CONICET PIP 11220090100457) and MINCYT-FWO International Exchange Project FW/09/03 is also acknowledged.

References

[1] Y. Fu, H. Du, W. Huang, S. Zhang, M. Hu, TiNi-based thin films in MEMS applications: a review, Sensors Actuators A 112 (2004) 395–408.
[2] M. Cai, S.C. Langford, M. Wu, W. Huang, G. Xiong, T.C. Droubay, A.G. Joly, K.M. Beck, W.P. Hess, J.T. Dickinson, Study of martensitic phase transformation in a NiTiCu Thin-film shape-memory alloy using photoelectron emission microscopy, Adv. Funct. Mater. 17 (2007) 161–167.
[3] H. Kahny, M.A. Huffz, A.H. Heuery, The TiNi shape-memory alloy and its applications for MEMs, J. Micromech. Microeng. 8 (1998) 213–221.
[4] F.C. Lovey, A.M. Condó, J. Guimpel, M.J. Yacamán, Shape memory effect in thin films of a CuAlNi alloy, Mater. Sci. Eng. A 481–482 (2008) 426–430.
[5] F. Wang, S. Doi, K. Hosoiri, H. Yoshida, T. Kuzushima, M. Sasadaira, T. Watanabe, Nanostructured Fe–Pd thin films for thermoelastic shape memory alloys: electrochemical preparation and characterization, Electrochim. Acta 51 (2006) 4250–4254.
[6] N. Haberkorn, M. Ahlers, F.C. Lovey, Tuning of the martensitic transformation temperature in Cu–Zn thin films by control of zinc vapor pressure during annealing, Scr. Mater. 61 (2009) 821–824.
[7] N. Haberkorn, F.C. Lovey, A.M. Condó, J. Guimpel, Development and characterization of shape memory Cu–Zn–Al thin films, Mater. Sci. Eng. B 70 (2010) 5–8.
[8] J. San Juan, M.L. Nó, C.A. Schuh, Superelastic cycling of Cu–Al–Ni shape memory alloy micropillars, Acta Mater. 60 (2012) 4093–4106.
[9] K. Otsuka, C.M. Wayman, Shape Memory Materials, Cambridge University Press, 1998.
[10] T. Minemura, H. Andoh, Y. Kita, I. Ikuta, Shape memory effect and microstructures of sputter-deposited Cu–Al–Ni films, J. Mater. Sci. Lett. 4 (1985) 793–796.
[11] V. Recarte, R.B. Pérez-Sáez, E.H. Bocanegra, M.L. Nó, J. San Juan, Dependence of the martensitic transformation characteristics on concentration in Cu–Al–Ni shape memory alloys, Mater. Sci. Eng. A 273–275 (1999) 380–384.
[12] V. Recarte, O.A. Lambri, R.B. Pérez-Sáez, M.L. Nó, J. San Juan, Ordering temperatures in Cu–Al–Ni shape memory alloys, Appl. Phys. Lett. 70 (1997) 3513–3515.
[13] J.I. Pérez-Landazábal, V. Recarte, R.B. Pérez-Sáez, M.L. Nó, J. Campo, J. San Juan, Determination of the next-nearest neighbor order in β phase in Cu–Al–Ni shape memory alloys, Appl. Phys. Lett. 81 (2002) 1794–1796.
[14] E. Zelaya, D. Schryvers, Reducing the formation of FIB induced FCC layers on Cu–Zn–Al austenite, Microsc. Res. Tech. 74 (2011) 84–91;
E. Zelaya, D. Schryvers, FCC surface precipitation in Cu–Zn–Al after low lngle Ga^{+} ion irradiation, Mater. Trans. 51 (2010) 2177–2180;
P.C. Wo, P.R. Munroe, M. Vasiliev, Z.H. Xie, K. Alameh, V. Kotov, A novel technique for microstructure characterization of garnet films, Opt. Mater. 32 (2009) 315–322.
[15] A. Hammersley, FIT2D V12.077, ESRF, 2005.
[16] ACC — version 6.0, users manual, SOFO, Brno, 2008.
[17] P. Stadelmann, EMS — a software package for electron diffraction analysis and HREM image simulation in materials science, Ultramicroscopy 21 (1987) 131–145.
[18] P. Molnár, P. Sittner, V. Novak, P. Lukas, Twinning processes in Cu–Al–Ni martensite single crystals investigated by neutron single crystal diffraction method, Mater. Sci. Eng. A 481–482 (2008) 513–517.
[19] A. Ibarra, D. Caillard, J. San Juan, M.L. Nó, Martensite nucleation on dislocations in Cu–Al–Ni shape memory alloys, Appl. Phys. Lett. 90 (2007) 101907–101910.
[20] G. Petzow, G. Effenberg, Ternary Alloys, 5, VCH, New York, 1992, pp. 615–625.
[21] M. Ahlers, The martensitic transformation: mechanisms and crystallography, Philos. Mag. A 8 (2002) 1093–1114.
[22] S.R. Yedurua, A. Backen, A. Fähler, L. Schultz, M. Kohl, Transformation behaviour of freestanding epitaxial Ni–Mn–Ga films, J. Alloys Compd. 577S (2013) 353–357.
[23] J.B. Liu, D.D. Johnson, BCC-to-HCP transformation pathways for iron versus hydrostatic pressure: coupled shuffle and shear modes, Phys. Rev. B 79 (2009) (134113–131122).
[24] K.F. Hane, T.W. Shield, Microstructure in a copper–aluminum–nickel shape-memory alloy, Proc. R. Soc. A 455 (1999) 3901–3915.
[25] C.S. Barrett, T.B. Massalski, Structure of Metals, 3rd ed. McGraw-Hill, New York, 1980.
[26] P. Arneodo Larochette, A.M. Condó, J.L. Pelegrina, M. Ahlers, On the stability of the martensitic phases in Cu–Zn–Al, and its relationship with the equilibrium phases, Mater. Sci. Eng. A 438–440 (2006) 747–750.
[27] R. Romero, J.L. Pelegrina, Change of entropy in the martensitic transformation and its dependence in Cu-based shape memory alloys, Mater. Sci. Eng. A354 (2003) 243–250.